

Topology-inspired Cross-domain Network for Developmental Cervical Stenosis Quantification

Zhenxi Zhang, Yanyang Wang, Yao Wu and Weifei Wu

Abstract—Developmental Canal Stenosis (DCS) quantification is crucial in cervical spondylosis screening. Compared with quantifying DCS manually, a more efficient and time-saving manner is provided by deep keypoint localization networks, which can be implemented in either the coordinate or the image domain. However, the vertebral visualization features often lead to abnormal topological structures during keypoint localization, including keypoint distortion with edges and weakly connected structures, which cannot be fully suppressed in either the coordinate or image domain alone. To overcome this limitation, a keypoint-edge and a reparameterization modules are utilized to restrict these abnormal structures in a cross-domain manner. The keypoint-edge constraint module restricts the keypoints on the edges of vertebrae, which ensures that the distribution pattern of keypoint coordinates is consistent with those for DCS quantification. And the reparameterization module constrains the weakly connected structures in image-domain heatmaps with coordinates combined. Moreover, the cross-domain network improves spatial generalization by utilizing heatmaps and incorporating coordinates for accurate localization, which avoids the trade-off between these two properties in an individual domain. Comprehensive results of distinct quantification tasks show the superiority and generability of the proposed Topology-inspired Cross-domain Network (TCN) compared with other competing localization methods.

Index Terms—Development cervical stenosis, Cross-domain keypoint localization, Topology feature, Keypoint-edge constraint, Reparameterization

I. INTRODUCTION

DEVELOPMENT Cervical Stenosis (DCS) is first defined by Hinck et al. in 1964 [1], referring to the narrowing of the cervical spinal canal in the process of development. Due to the short development of the spinal canal, the spinal cord and nerve roots will be stimulated or compressed [2], leading to severe cervical spondylosis [3], [4]. Epidemiological studies have revealed that the incidence of DCS within the general population ranges from 5% to 20% [5]. The severe complication and high incidence emphasize the need for further investigation into DCS quantification for timely prevention.

Z. Zhang and Y. Wang are with the Department of Biomedical Engineering, Sun-Yat-sen University, Shenzhen Campus, Shenzhen, China (e-mail: zhangzhx37@mail2.sysu.edu.cn, wangyy378@mail2.sysu.edu.cn). Y. Wu is with the Clinical Medicine of the Three Gorges University, Yichang, China (e-mail: wybone2023@163.com). W. Wu is with the Department of Orthopedics, the affiliated Hospital of China Three Gorges University, Yichang, China. W. Wu is the corresponding author (e-mail: spinedeform2018@sina.com).

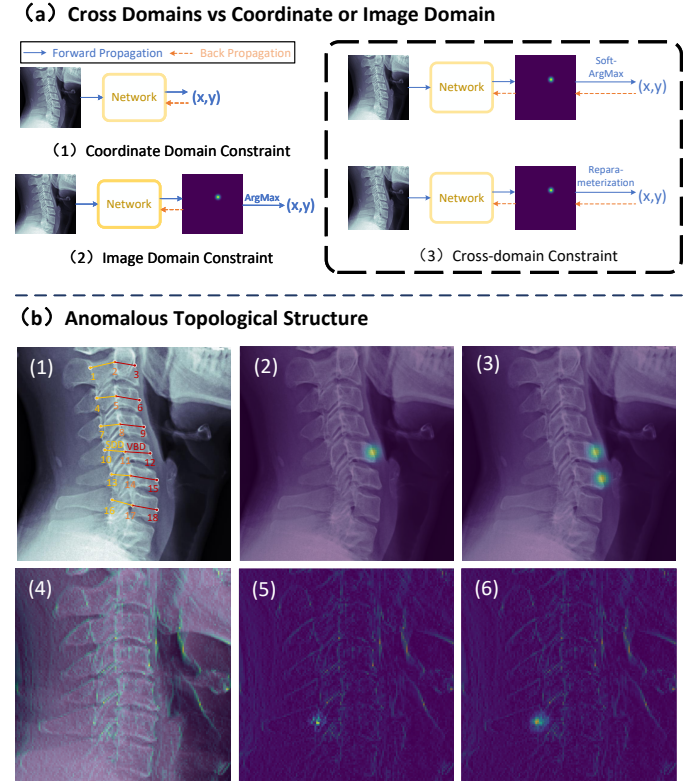


Fig. 1. The architecture of cross-domain keypoint localization and the anomalous topological structure in heatmaps. (a) lists the cross-domain method in comparison with the conventional coordinate domain and the image domain methods. (b)(1) shows 18 keypoints in total related to SDD and VBD. (b)(3) exhibits the abnormal connected structure in heatmaps compared with (b)(2). (b)(4) shows the CT image of the cervical spine enhanced by the edge. And Compared with (b)(6), (b)(5) reflects the topological distortion of a keypoint with respect to an edge.

Although effective, the conventional manual quantification method for DCS is time-consuming and dependent on the clinical experience of doctors. In this method, the Sagittal Developmental Diameter (SDD) and the Vertebral Body Diameter (VBD) of each vertebra are measured. A patient is considered to have DCS if the ratio of SDD to VBD of the same vertebra is less than 0.75 [6]. This is illustrated in Figure 1 (b)(1), where the yellow and red lines represent SDD and VBD, respectively. However, the process of annotating SDD and VBD by spinal surgeons takes approximately 3 minutes per patient, making it impractical for large-scale DCS screening. Additionally, the accuracy of this annotation relies on the identification of spinal corticomedullary margins [5], which will be influenced by the

quality of CT imaging. And measuring SDD and VBD on blurred spinal margins requires surgeons to possess substantial clinical experience.

Deep networks offer a significant reduction in the medical image processing time compared to the manual quantification method, providing a robust foundation for large-scale screening. These networks have been extensively investigated for various spinal quantification tasks, such as fracture detection [7] and lumbar spinal stenosis [8]. In the case of DCS, which requires the measurement of SDD and VBD using three keypoints per vertebra, deep keypoint localization networks are employed. These localization networks not only assist surgeons in interpretable DCS quantification using keypoints but also alleviate the time-consuming task of processing CT images. Specifically, spinal localization networks can efficiently locate keypoints on vertebrae and calculate SDD/VBD within a matter of seconds. Based on the representation of keypoints, spinal localization networks can be implemented in the coordinate domain and the image domain. In the coordinate domain (Fig.1(a)(1)), keypoint coordinates are regressed [9], [10], while in the image domain (Fig.1(a)(2)), keypoint heatmaps are constrained [7], [11], [12]. Here, heatmaps for training are generated by placing a spherical 2D Gaussian at the ground truth coordinates.

However, during the process of localizing keypoints on vertebrae, the vertebral visualization features can lead to anomalous topological structures, including keypoint distortion with respect to edges and weakly connected structures. These structures cannot be fully resolved in either the coordinate domain or the image domain alone. Topological keypoint distortion in DCS quantification refers to the situation where the DCS keypoint does not align with the vertebral edges (as shown in Fig.1(b)(6)). Edges are not easily represented by coordinates, limiting the relations between keypoints and edges in the coordinate domain [13]. Additionally, the presence of weakly connected structures (as shown in Fig.1(b)(3)) affects DCS quantification as well. In mathematics, a space (Ω) is considered to be connected if there is a continuous path between any two points within that space, without any breaks or disjointed components. In keypoint heatmaps, the space is determined based on grayscale values (p_i), with $\Omega : p_i > th$, where th is a manually set threshold. To ensure connectivity, a small value of th can be only chosen for weakly connected structures, while a larger value can be used for strongly connected structures. Weakly connected structures arise due to the similarity in visualization features among vertebrae, commonly appearing in the heatmaps of the image domain (as shown in Fig.1(b)(3)). Particularly, conventional heatmap-based models typically employ the Mean Squared Error (MSE) as the loss function to update parameters [7], [11], [12]. In this case, all the regions in heatmaps are evaluated with the same weight, and the regions of different vertebrae are wrongly activated due to the high visual similarity [14]. To preserve the strongly connected structures in the heatmaps, keypoint coordinates are needed to suppress activations on incorrect vertebrae by assigning higher weights to regions farther from keypoints.

In this paper, we propose a topology-inspired network

for DCS quantification cross the image and coordinate domains. The keypoint-edge and reparameterization modules are adopted in the network to process the keypoint distortion and weakly connected structures. Precisely, considering the fact that all the keypoints are located closely to the corticomedullary margin of vertebrae [5], a keypoint-edge constraint module is designed to prevent the topological distortion of keypoints. This module combines keypoint heatmaps and edge operators to generate edge maps (as exhibited in Fig.1(b)(4)) of vertebrae. By integrating edge maps and heatmaps, our proposed method overcomes the limitations of applying either approach alone. Specifically, traditional edge operators applied in edge maps are sensitive to blurred edges, leading to less accurate edge detection [15]. On the other hand, relying solely on heatmaps requires a substantial number of keypoints [13], which can be time-consuming to annotate in medical datasets. Our approach effectively addresses these drawbacks, resulting in more robust and accurate edge maps, as shown in Fig. 1(b)(4). After being restricted by edge maps, processed heatmaps (shown in Fig. 1 (b)(5)) avoid the topological distortion and improve the location precision with subsequent reparameterization. To be specific, reparameterization maps heatmaps to coordinates in a mathematical manner, ensuring that the relations between keypoints and edges in the heatmap can be interpretably transmitted to coordinates. These coordinates are subsequently incorporated with heatmaps to construct a new topological loss for strongly connected structures. Based on mathematical analysis in Section III-C, reparameterization enables the new loss function to be easily derived. Furthermore, the proposed method is cross-domain, avoiding a trade-off between spatial generalization and precise location in comparison with the image domain or the coordinate domain approach. Here, spatial generalization refers to the ability to generalize knowledge from one training location to another location during inference [16]. And this point is manifested in inferring abnormal keypoints of deformed vertebrae. In the coordinate-based network, coordinates are useful for precise localization after end-to-end training, directly generating these coordinates from images with a neural network may lead to overfitting and affect the spatial generalization [17]. Although spatial generalization can be preserved by removing the process from the image domain to the coordinate domain with a neural network in the heatmap-based approach, the similarity of keypoint location and its adjacent regions in heatmaps may result in inaccurate analysis of keypoint locations with Argmax [16]. As shown in Fig. 1 (a)(3), the cross-domain method transforms medical images into heatmaps, and then generates coordinates through a differentiable and non-parameter projection. By achieving this, the proposed method preserves spatial generalization while transforming the image domain to the coordinate domain, enabling accurate localization using numerical coordinates as output.

To demonstrate the superiority and generability of our proposed TCN, multiple quantification methods based on keypoints are employed to evaluate in vertebral quantification task, including DCS and scoliosis. The quantification results confirm that our method outperforms other competing

keypoint-based methods. Our contribution can be summarized as follows:

- We propose a keypoint-based quantitative model to assist DCS diagnosis for the first time. And the keypoints provide interpretability for clinical DCS quantification.
- The suppression of abnormal topological structures is utilized to improves the performance of the keypoint-based DCS quantification. Specifically, a differentiable and parameter-free reparameterization module is applied to suppress the abnormal connected structure in heatmaps. And a keypoint-edge constraint module to prevent the topological distortion of keypoints.
- The cross-domain method balances strong generalization and high precision for DCS quantification. Precisely, the reparameterization module is utilized to bridge coordinate and image domains. The spatial generalization is reserved by obtaining coordinates from the image domain in a parameter-free manner, and accurate localization is incorporated with output numerical coordinates.
- The superiority and generability of our proposed method have been extensively verified in two vertebral quantification tasks. Comparing with other competing keypoint-based quantification methods, our proposed method can obtain the best performance.

II. RELATED WORK

A. DCS Quantification

The conventional method for DCS quantification involves manual measurement of SDD and VBD [6]. While the conventional manual quantification method is effective, it is also time-consuming. To address this issue, CNN classifiers have been employed for quantifying spinal canal stenosis [8], [18]. Additionally, attention maps are utilized in these classifiers to visualize the focus areas of the models, thereby enhancing the reliability of the classifier [8], [18]. However, despite highlighting regions of interest, the interpretability of the decision-making process between attention maps and the quantification results is limited with complex projection, making it challenging for surgeons to understand the final outcomes [19]. In our approach, heatmaps are applied to depict the regions of interest identified by the models. To retain the interpretability, a differential mathematical projection is employed to convert the heatmaps into keypoint coordinates, enabling accurate SDD and VBD for DCS quantification.

B. Vertebral Keypoint Localization

It aims to quantify vertebral indexes intuitively and interpretably. It is important clinically for computer-aided diagnosis of vertebral disease via quantification. Early methods extract coordinates from medical images directly and the distance correlations of keypoints can be restricted simultaneously for accurate quantification [9], [10]. Although the morphological indices can be precisely evaluated end-to-end, the lack of spatial generalization will lead to insensitive to abnormal keypoints [16]. This becomes particularly evident when inferring abnormal keypoints on deformed vertebrae. In order to improve the spatial generalization, some works attempt on

replacing the coordinates with Gaussian heatmaps of image domain [11], [12]. The spatial generalization will be reserved by displacing the intra-domain constraint with inter-domain constraint. While the heatmap-based approach has strong spatial generalization to localize keypoints on severely distorted vertebrae, it is limited by the undifferentiable operation that transforms heatmaps to corresponding coordinates by Argmax. In addition to the undifferentiable operation, the keypoints have similar values with their adjacent regions in heatmaps, leading to inaccurate analysis of keypoint locations and correlations. Balancing spatial generalization and accuracy by bridging the image domain and the coordinate domain is an intuitive idea. Soft-Argmax function meets this requirement by locating the coordinates of the maximum value from a heatmap [16]. However, the soft-Argmax function is to calculate the expectation value, which is difficult to reflect the optimal coordinate in heatmaps with anomalous topological structure of vertebrae. The reason is that the soft-Argmax function is unable to handle the anomalous topological structure of heatmaps, as illustrated in Fig.1(b)(3) and Fig.1(b)(5).

C. Vertebral Topological Structure

1) *Strongly Connected Structure*: It is one of the topological structures visualized in standard heatmaps (in Fig.1 (b)(2)). In vertebral images, this structure is frequently destroyed due to similar vertebral appearances (in Fig.1 (b)(3)). Early works adopt domain expert knowledge to categorize and then process vertebrae separately [20], [21]. Although the wrong localization caused by similar vertebral appearances can be suppressed, however, due to the absence of spatial relations between vertebrae, the cross-vertebra morphological indices cannot be accurately evaluated. To improve the spatial relations with fewer effects of similar vertebral appearances reserved, Markov [22] and Recurrent Neural Network (RNN) [23], [24] models are respectively adopted to localize vertebral keypoints by retaining the consecutive order. Even though these sequential methods are effective to add spatial relations, they are limited the fact that the keypoints are mainly restricted by their neighboring ones. In order to impose the global spatial relations of keypoints, the arc-length parameterization has been implemented by Wang to constrain keypoints on a curve [14]. Besides, an anatomically-constrained optimization is designed to reduce the influence of similar vertebral appearances with an iterative operation. However, the iterative operation required for the anatomically-constrained optimization inevitably results in a large amount of training and inference time consumption.

2) *Keypoint-edge Topological Relation*: It is applied to constrain the network with the topological structure between vertebral keypoints and edges. Previous works on face keypoint detection have estimated facial edges that are applied in the topological structure with dense ground truth keypoints. The predicted coordinates [13] or heatmaps [26], [27] are then constrained by these edges to satisfy facial shapes. While restricting keypoints with edges has shown promising results for face detection, this approach is limited in medical quantification where keypoints for localization are too sparse to

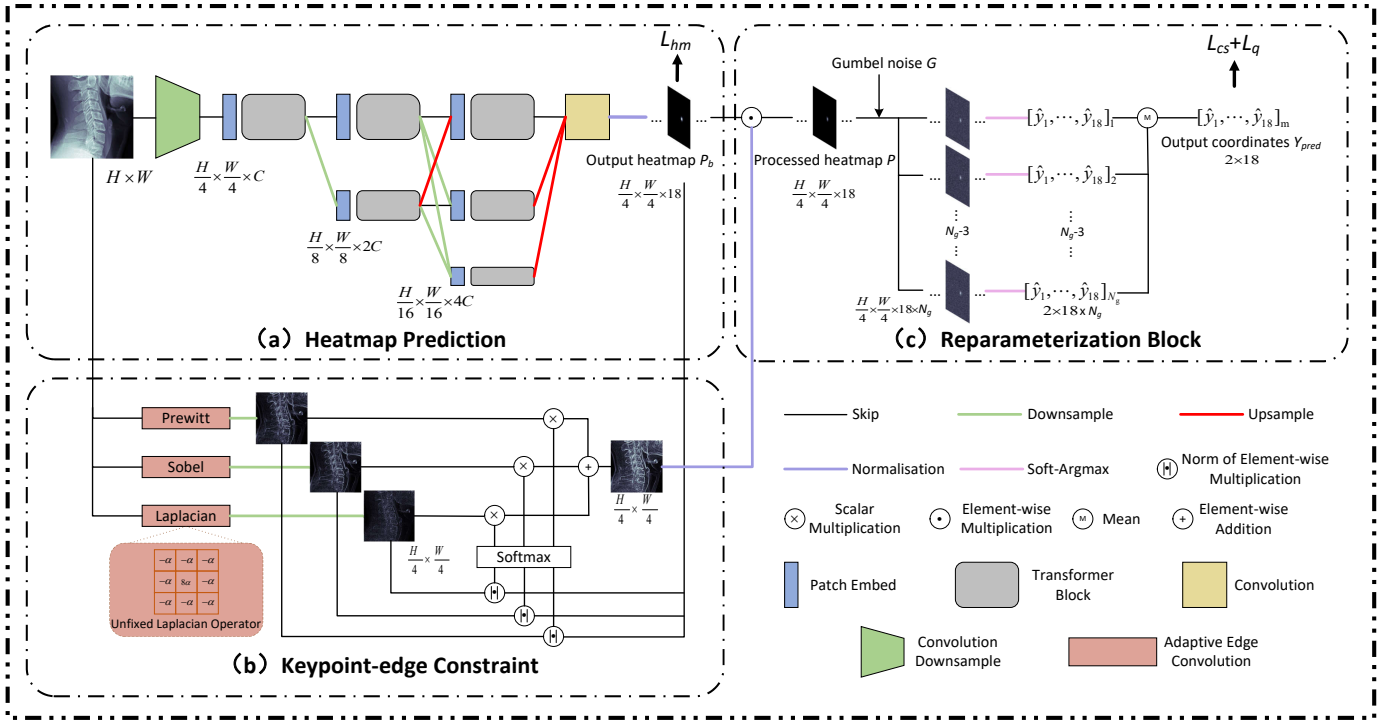


Fig. 2. The overall architecture of our proposed TCN. (a) The heatmap prediction with HRViT [25] as backbone. (b) The keypoint-edge constraint module. (c) The reparameterization block.

build edges. Specifically, denoting a large number of keypoints to create edges may result in redundancy, making it difficult to select keypoints for quantification. Additionally, the edges in CT images may not be distinctive enough to be denoted by keypoints manually due to the noise captured in the CT device and image reconstruction process [28]. To address the challenge of processing these blurred edges, an adaptive Sobel operator has been designed for sparse-view tomographic reconstruction [15]. Although not directly related to keypoint localization, this article has inspired us to develop an edge extraction method for blurry edges without the need for extra keypoints.

III. METHOD

The proposed TCN consists of three modules, including heatmap prediction, keypoint-edge constraint and reparameterization. The strongly connected structure in heatmaps is guaranteed with the new topological loss. And this loss is combined with heatmaps and coordinates from HRViT backbone (shown in Fig.2 (a)) and reparameterization block (shown in Fig.2 (c)), respectively. The keypoint-edge constraint module (shown in Fig.2 (b)) is designed based on the priori knowledge of the keypoints location of DCS should be on the edges, which can prevent the topological distortion of keypoints with edges.

A. Heatmap Prediction

HRViT [25] is applied as the backbone network to predict the heatmap of vertebral keypoints. In Fig.2 (a), HRViT adopts a parallel high-to-low resolution subnetworks rather than a serial structure of high-to-low resolution in UNet [29], ResNet [30] and FCN [31]. The parallel structure can maintain high

image resolution with end-to-end way, reducing the resolution loss in the serial structure [32]. Additionally, HRViT [25] has strong ability of modeling long-range interaction similar to ViT [33], which is helpful to explore relationships of different keypoints.

B. Keypoint-edge Constraint

In light of the topological priori knowledge that keypoints for DCS diagnosis should be on the edges of the vertebrae, a topology constraint module is designed. Different from conventional fixed-value edge operators, inspired by [15], we adopt multiple operators (exhibited in the red box of Fig.2 (b)) for dynamic edge adjustment. Specifically, we incorporate a trainable parameter α , into the edge operator to balance the intensity of the corresponding edge maps. The keypoint-edge constraint is implemented with three steps. As edges of vertebrae exhibit varying morphologies and grayscale features, we first leverage three trainable edge operators – Prewitt, Sobel and Laplacian – to extract the vertebral edges. Subsequently, the degree of overlap of three edge maps is determined by using the dot products of the keypoint heatmap individually. The three edge maps are weighted merged with the overlap. Here, the weights of three edge maps can be adaptive adjusted during training process with relying on the trainable parameter α in the edge operator. Finally, the weighted edge map is normalised and multiplied with the Gaussian heatmap to restrict the topological relations between keypoints and vertebral edges.

C. Reparameterization Block

Reparameterization is designed to suppress the weakly connected structures in the vertebral heatmaps. It also bridges the image and coordinate domains, similar to soft-Argmax. For soft-Argmax, its output coordinates L_{pred} and corresponding coordinate loss L_c can be respectively expressed as:

$$y_{pred} = \text{Soft-Argmax}(P) = \sum_{i=1}^n p_i y_i, \quad (1)$$

$$L_c = \|y_{gt} - y_{pred}\|_1, \quad (2)$$

where P is the heatmap after topology constraint, y_i and p_i represents the index and context of the i -th location from heatmap P respectively. In fact, every heatmap reflects the probability of a single keypoint at different locations. The soft-Argmax provides a differentiable way to find the location with the highest probability of the heatmap. However, for the anomalous connected structure shown in Fig.1 (b)(3), y_{pred} from soft-Argmax is not the location with the highest probability. To solve this problem, we need to add the connected structure of the heatmap to coordinate loss L_c . Inspired by [34], the connected-structure-based coordinate loss L_{cs} and its gradient $\nabla_\theta L_{cs}$ can be written as:

$$L_{cs} = \sum_{i=1}^n p_i \|y_{gt} - y_i\|_1, \quad (3)$$

$$\nabla_\theta L_{cs} = \sum_{i=1}^n \|y_{gt} - y_i\|_1 \nabla_\theta p_i = E_y(\|y_{gt} - y\|_1 \nabla_\theta \log(P)) \quad (4)$$

where E represents the mathematical expectation and θ is the optimization model parameter. By optimizing new coordinate loss L_{cs} , P will gradually become a heatmap with only one peak indicating the maximum value at y_{gt} . However, $\|y_{gt} - y_i\|_1$ in $\nabla_\theta L_{cs}$ is independent of model parameters θ and has a large variance, making L_{cs} is difficult to converge [34].

The reparameterization is applied to estimate $\nabla_\theta L_{cs}$ in a sampling-based manner. Comparing to directly sampling \hat{y} in P , reparameterization is differentiable owing to decoupling the sampling operation from network computations. Gumbel-Softmax [35] is a reparameterization method to handle discrete probability distributions, it is adopted to sample \hat{y} from heatmap P for estimating L_{cs} . The estimation process can be divided into two steps:

The first step is adding the Gumbel noise to P , and then we select the position with the largest value as sampling output \hat{y} . Specifically, this step is expressed as:

$$g_i = -\log(-\log(\zeta_i)) \quad \zeta_i \sim U(0, 1), \quad (5)$$

$$\hat{p}_i = \frac{\exp((\log(p_i) + g_i)/\tau)}{\sum_{j=1}^n \exp((\log(p_j) + g_j)/\tau)}, \quad (6)$$

$$\hat{y} = \text{soft-Argmax}(\hat{P}), \quad (7)$$

where g denotes the Gumbel noise, $U(0, 1)$ is a uniform distribution ranging from 0 to 1, τ is the Softmax temperature

and \hat{P} is the heatmap P with Gumbel noise. If $\hat{y} = y_i$ in Eq. 7, \hat{p}_i is the maximum value in \hat{P} . That means:

$$\begin{aligned} \ln(p_i) - \ln(\ln(\zeta_i)) &> \ln(p_1) - \ln(\ln(\zeta_1)), \\ \ln(p_i) - \ln(\ln(\zeta_i)) &> \ln(p_2) - \ln(\ln(\zeta_2)), \\ &\dots \\ \ln(p_i) - \ln(\ln(\zeta_i)) &> \ln(p_j) - \ln(\ln(\zeta_j)), \\ &\dots \end{aligned} \quad (8)$$

where $j = 1, 2, \dots, n$ and $j \neq i$. From the first formula of Eq. 8, it can deduce:

$$\begin{aligned} \frac{p_i}{\ln(\zeta_i)} &< \frac{p_1}{\ln(\zeta_1)} \\ \ln(\zeta_1) &< \frac{p_1}{p_i} \ln(\zeta_i) \\ \zeta_1 &< [e^{\ln(\zeta_i)}]^{\frac{p_1}{p_i}} \\ \zeta_1 &< \zeta_i^{\frac{p_1}{p_i}}. \end{aligned} \quad (9)$$

Considering that ζ_1 comes from a uniform distribution ranging from 0 to 1, the probability that the first inequality in Eq. 8 holds is $\zeta_i^{\frac{p_1}{p_i}}$. Then, the probability that all inequalities in Eq. 8 hold at the same time is:

$$P(\hat{y} = y_i) = \prod_{j=1, j \neq i}^n \zeta_i^{\frac{p_j}{p_i}} = \zeta_i^{\frac{\sum_{j=1, j \neq i}^n p_j}{p_i}} = \zeta_i^{\frac{1}{p_i} - 1}. \quad (10)$$

If $P(\hat{y} = y_i)$ is repeatedly sampled and its average is calculated, the Law of Large Numbers guarantees that the average of $P(\hat{y} = y_i)$ will converge to the expected value of $E(P(\hat{y} = y_i))$:

$$E(P(\hat{y} = y_i)) = \int_0^1 \zeta_i^{\frac{1}{p_i} - 1} d\zeta_i = p_i. \quad (11)$$

From Eq. 11, it can be known that reparameterization makes $S(\hat{y} = y_i) = E(P(\hat{y} = y_i)) = p_i$ hold and $S(\hat{y} = y_i)$ differentiable by sampling ζ .

In the second step, L_{cs} and its gradient $\nabla_\theta L_{cs}$ are respectively calculated by:

$$L_{cs} \approx \frac{1}{N_g} \sum_{k=1}^{N_g} \|y_{gt} - \hat{y}_k\|_1, \quad (12)$$

$$\nabla_\theta L_{cs} = \nabla_\theta E_{\hat{y}}(\|y_{gt} - \hat{y}\|_1) = E_G\left(\frac{\partial \|y_{gt} - \hat{y}\|_1}{\partial \hat{y}} \frac{\partial \hat{y}}{\partial P} \frac{\partial P}{\partial \theta}\right), \quad (13)$$

where N_g is the number of Gumbel sampling and G is multivariate Gumbel distribution composed by g_i in Eq.5. Actually, the $\nabla_\theta L_{cs}$ passing through reparameterization can be easily computed during training. Moreover, when $\nabla_\theta L_{cs}$ and shape constraint are no longer needed in testing, the reparameterization can be replaced by soft-Argmax without randomness introduced.

D. Loss Function

The final loss function is the sum of three components, including coordinate loss with shape constraint L_{cs} , heatmap loss L_{hm} and quantification loss L_q . Specifically, L_{cs} is listed in Eq.12, L_{hm} is evaluated by Kullback-Leibler divergence

D_{KL} with reference to [16] and L_q is calculated to constrain SDD and VBD. L_{hm} and L_q are respectively represented as:

$$L_{hm} = D_{KL}(P_b, P_{gt}), \quad (14)$$

$$L_q = \beta(d(LS_{pred}, LS_{gt}) + d(LV_{pred}, LV_{gt})) - (R_{pred} - \gamma)(R_{gt} - \gamma), \quad (15)$$

where P_b is the output heatmap from backbone, LS and LV denote the the length of SDD and VBD respectively, R is LS divided by LV , β is a hyperparameter gradually increasing from $1e^{-5}$ to $1e^{-2}$ during training, d represents the L_1 -distance and γ is the threshold to diagnose DCS, set as 0.75 referred to Lim [6].

TABLE I

DCS QUANTIFICATION WITH VERTEBRAL KEYPOINT LOCALISATION METHODS.

Method	Specificity	Sensitivity	Accuracy
Coordinate Domain Constraint			
DenseNet [36]	92.05%	14.49%	57.96%
InceptionNet [37]	93.18%	16.53%	58.60%
ViT [33]	90.91%	18.84%	59.24%
ResNet [30]	93.18%	52.17%	75.16%
Image Domain Constraint			
UNet [29]	86.36%	68.12%	78.34%
CPN [38]	92.05%	69.57%	82.17%
HRNet [39]	89.77%	75.36%	83.44%
HRViT [25]	93.18%	73.91%	84.71%
Cross Domain Constraint			
DSNT [16]	92.05%	78.26%	85.99%
TCN	94.32%	81.16%	88.54%

TABLE II

SCOLIOSIS ASSESSMENT ON AASCE [40].

Method	Input Resolution	SMAPE
Multi-view Extrapolation Net [41]	512×256	23.43
Residual UNet [42]	1024×512	16.48
Keypoint Detection Network [11]	1024×512	10.96
TCN	1024×512	10.00

IV. EXPERIMENT

A. Dataset

The topology-inspired network is evaluated on two vertebral datasets: an in-house dataset for DCS quantification and the public AASCE [40] datasets for scoliosis assessment. In each dataset, keypoints are localized on vertebral margins and influenced by similar vertebral appearances.

The DCS dataset comprises 1,623 patients as well as 1,623 cervical sagittal CT images. In respect to the datasets, 203 out of 1,623 subjects are diagnosed with DCS. In our experiments, 1,466 and 157 of 1,623 subjects are used as training and testing datasets respectively. Especially, for better evaluating the generalization and accuracy of the quantification model, the test datasets need to be well designed. Here, 67 out of 157 subjects are diagnosed with DCS, and the remaining 90 are normal subjects. According to the [6], 18 keypoints are located on $C2 \sim C7$ vertebrae. That means an 18-channel Gaussian heatmap P_{gt} can be generated as the ground truth. Similar to

[43]–[45], the ground truth heatmap is constructed by using $P_{gt} = \exp\left(\frac{-\|y - y_{gt}\|_2^2}{2\sigma^2}\right)$, where σ controls the spread of the Gaussian heatmap, and it was set as 1.5 in our experiments.

The public AASCE dataset [40] contains 609 anterior-posterior X-ray images for quantifying scoliosis. Specifically, out of these images, 365 were used for training, 116 for validation, and 128 for testing. In every image, 17 vertebrae are marked on the thoracic and lumbar spine, with each vertebra localized using four corner keypoints. Following Wang [40], the Cobb angle is evaluated by the symmetric mean absolute percentage error (SMAPE) to assess scoliosis. Specifically, SMAPE is measured by using $SMAPE = \frac{1}{N} \sum_{j=1}^N \frac{\sum_{i=1}^3 (|a_{ji} - b_{ji}|)}{\sum_{i=1}^3 (|a_{ji} + b_{ji}|)}$, where i indexes the three Cobb angles in the proximal thoracic (PT), main thoracic (MT), and thoracolumbar (TL) areas, j denotes the j^{th} image, and N represents the total number of testing images. The variables a and b correspond to the predicted and ground-truth Cobb angles, respectively.

B. Implementation Details

All networks are implemented with Pytorch framework on Nvidia A100 and adopt Adam [46] to optimize nerwork. The learning rates for DCS and AASCE datasets are set to $5e^{-3}$ and $1.25e^{-4}$, respectively. The iteration is terminated at the 150th epoch on DCS, and 70th epoch on AASCE [40].

The images in the DCS dataset undergo cropping to a size of 512×512 pixels before training. Additionally, image augmentation includes random horizontal flips with a 0.5 probability, as well as random rotation shifts within the range of $[-\frac{\pi}{6}, \frac{\pi}{6}]$ and scaling within the range of [0.75, 1.25].

For the AASCE dataset [40], the input image resolution is fixed at 1024×512 pixels. Following Yi [11], a variety of standard data augmentation techniques are employed before training, including random expansion ranging from 1.0 to 1.5, contrast adjustments, and modifications in brightness levels.

C. Results

The proposed TCN is compared with several representative and state-of-the-art (SOTA) methods with coordinate or image domain constraint on DCS dataset shown in Table I. All the cross-domain networks, including DSNT [16] and proposed TCN, adopt HRViT [25] as the backbone. Here, the DSNT [16] is a cross-domain method based on soft-Argmax without vertebral topological structure considered. As can be seen, when topological structure constraint is applied in the proposed network, the performance are further improved in comparison with cross-domain DSNT [16]. Specifically, TCN attains an improvement of 2.55 percentage points over DSNT [16] in accuracy. Furthermore, the cross-domain approach is valid for balancing accurate diagnosis and spatial generalization. To be specific, the higher sensitivity of the image and cross-domain approaches in comparison with the coordinate domain methods proves the effectiveness of spatial generalization to process deformed vertebrae in patient group. When coordinates are incorporated with the image-domain approach in cross-domain networks, the performance of diagnosis are further improved.

TABLE III

ABLATION EXPERIMENTS. THE SA, RE, KEC, HDC, CDC AND AQE ARE RESPECTIVELY BRIEF EXPRESSION FOR SOFT-ARGMAX, REPARAMETERIZATION, KEYPOINT-EDGE CONSTRAINT, IMAGE DOMAIN CONSTRAINT, COORDINATE DOMAIN CONSTRAINT AND AVERAGE QUANTIFICATION ERROR. THE AQE IS EVALUATED BY THE MEAN ABSOLUTE ERROR OF SDD/VBD, AND GIVEN AS MEAN \pm STD IN THE LAST COLUMN.

Sa	Re	KeC	HDC	CDC	Specificity	Sensitivity	Accuracy	AQE
✓				✓	93.18%	68.12%	82.17%	0.054 \pm 0.051
			✓		93.18%	73.91%	84.71%	0.058 \pm 0.054
✓			✓	✓	92.05%	78.26%	85.99%	0.053 \pm 0.053
✓		✓	✓	✓	95.45%	78.26%	87.90%	0.052 \pm 0.049
	✓	✓	✓	✓	93.18%	79.71%	87.26%	0.051 \pm 0.052
✓	✓	✓	✓	✓	94.32%	81.16%	88.54%	0.050 \pm 0.050

These results demonstrate the necessity of the vertebral topological structure and combining the coordinate and image domain constraint with the proposed topological-inspired cross-domain method.

To assess the generability of the topology-inspired network, a keypoint detection network [11] is incorporated as the new backbone within the TCN, aimed at quantifying scoliosis with Cobb angles on the AASCE dataset [40]. The results in Table II unequivocally illustrate the impact of applying the topological constraint to the baseline network [11]. Notably, this constraint yields a substantial increase of 0.96 percentage point in SMAPE with only a few trainable parameters added. This significant advancement over the baseline underscores the efficacy of the proposed network in integrating topological information and potentially offering a generalized solution for diverse vertebral tasks.

D. Ablation Study

In this section, we have demonstrated the validity of the topological structure and the superiority of cross-domain constraint in DCS quantification. All models in this section are implemented with HRViT [25] as backbone.

Connected structure and keypoint-edge relation are two types of topological structures that are effective for vertebral keypoint localization. The reparameterization block enforces the connected structure, resulting in higher accuracy and lower AQE compared to models without reparameterization. This can be seen by comparing the 3rd and 4th rows with the 5th and 6th rows in Table III respectively. The keypoint-edge relation constrains the topological relationship between keypoints and edges, which leads to superior performance. This is demonstrated by respectively comparing the 3rd and 5th rows with the 4th and 6th rows in Table III. Fig. 3 visually illustrates the effectiveness of these topological structures. The red box and blue box in Fig. 3 demonstrate the abnormal connected structure generated by HRViT [25] and DSNT [16], respectively. Enforcing the connected structure constraint through reparameterization effectively suppresses the abnormal connected structures, as demonstrated in the last two columns of Table III. Meanwhile, the keypoint-edge constraint is enforced using adaptive vertebral edges (shown in the 5th column of Fig. 3). This results in more precise heatmaps, with their peaks concentrated in the vicinity of the vertebral edges (shown in the green box of Fig. 3).

The proposed TCN integrates coordinate and image domain constraints to balance accurate localization and spatial generalization. In Table III, the 1st and 2nd rows show the performance with coordinate and image domain constraints, respectively. The coordinate domain model has lower AQE and sensitivity compared to the image domain model. The lower AQE suggests that fully differential processing from images to coordinates benefits the accurate quantification. On the other hand, the higher sensitivity of the image domain method highlights its effectiveness in processing anomalous vertebrae, emphasizing the importance of spatial generalization. To achieve higher sensitivity and smaller AQE simultaneously, we introduce the image constraint as a supplement to the coordinate constraint in cross-domain models. As shown in the last four rows of Table III, cross-domain models exhibit superior performance based on the fusion of the two different constraints.

TABLE IV

COMPARISON OF PREDICTED AND GROUNTRUTH SDD/VBD VALUES. RADIOLOGIST AND MODEL REFER TO GROUNTRUTH AND PREDICTED SDD/VBD VALUES RESPECTIVELY, EXPRESSED AS THE MEAN \pm STD. ICC, PC AND P ARE RESPECTIVELY BRIEF EXPRESSION FOR INTRA-CLASS CORRELATION COEFFICIENT, PEARSON CORRELATION AND P VALUE.

Vertebra	Radiologist	Model	ICC	PC	P
C2	1.26 \pm 0.18	1.27 \pm 0.15	0.80	0.81	0.94
C3	0.92 \pm 0.14	0.91 \pm 0.13	0.89	0.90	0.67
C4	0.90 \pm 0.16	0.89 \pm 0.14	0.91	0.91	0.63
C5	0.93 \pm 0.16	0.91 \pm 0.15	0.94	0.94	0.32
C6	0.92 \pm 0.15	0.91 \pm 0.14	0.91	0.91	0.44
C7	0.89 \pm 0.15	0.87 \pm 0.13	0.81	0.82	0.38

V. DISCUSSION

A. The Assessment with Clinical Measures

This section evaluates SDD/VBD values applying clinical measures by comparing them with groundtruth from the radiologist. As shown in Table IV, the predicted values and groundtruth have similar mean and standard, with their P values exceeding 0.05. This suggests no significant difference between the prediction and groundtruth. Additionally, in Table IV, all ICC and PC values are greater than 0.80 (ICC 0.80-0.94, PC 0.81-0.94), indicating that the SDD/VBD predicted by the model for six vertebrae is consistent and reliable compared to the groundtruth. To intuitively illustrate

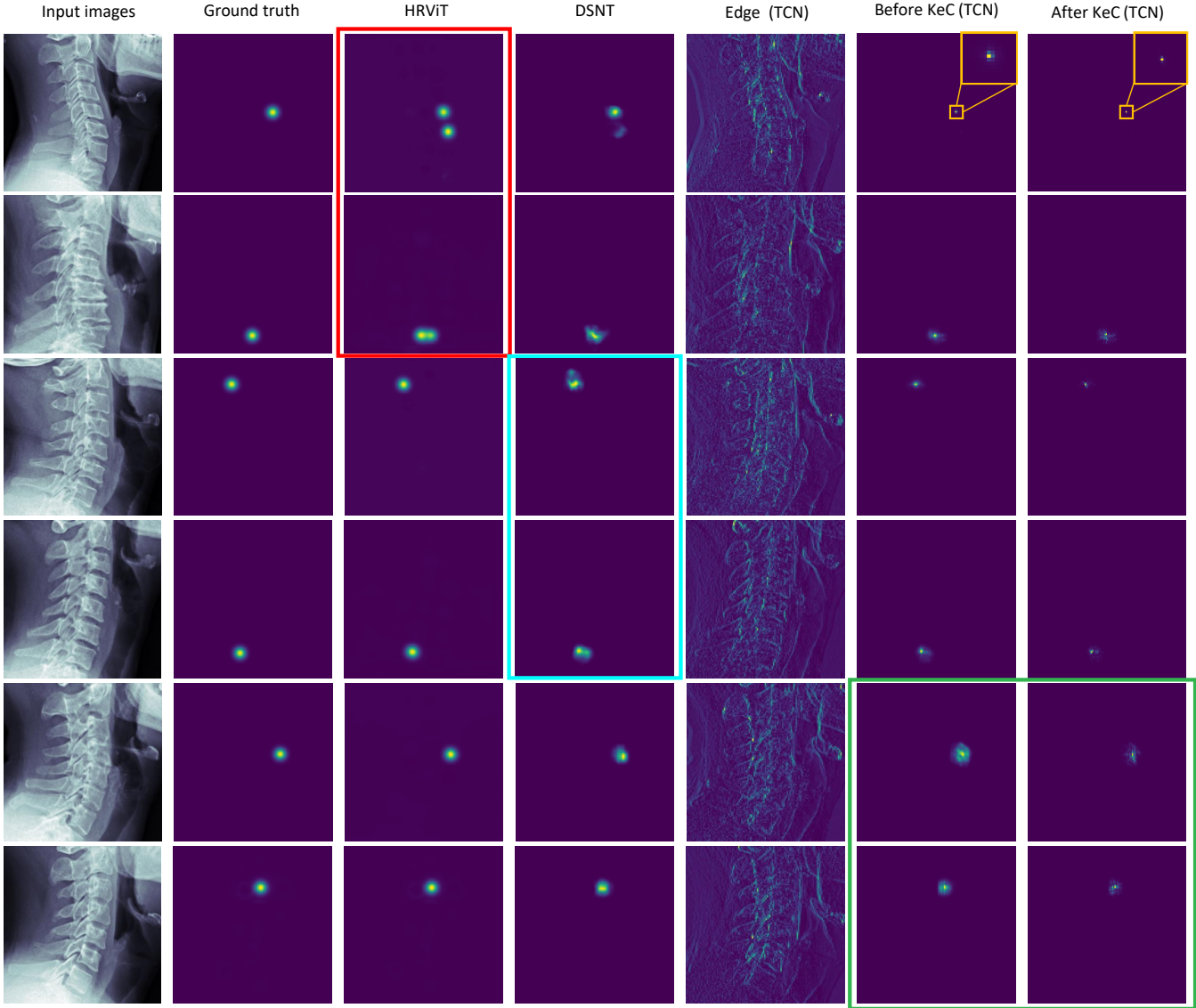


Fig. 3. The visualisation of heatmaps and edge maps. The 6th and 7th columns are the heatmaps before and after applying the Keypoint-edge constraint in TCN, respectively. The adaptive edge maps used are placed in the 5th column.

the consistency of quantification indices from the model and the radiologist, the correlation scatter diagrams and Bland-Altman plots are applied in Fig. 4. Specifically, scattered points mostly evenly distributed on a straight line indicate a strong correlation between predicted and groundtruth values. And the difference between these two values is not large, as shown by the fact that the points primarily fall within the 95% limit of agreement (LoA) between the reference standard and the model estimate measurements in Bland-Altman plots.

B. The Effect of Edge Operators

In this section, different operators are separately applied to explore their effect in keypoint-edge constraint on DCS dataset. As seen in Table V, four edge operators, including 'Laplacian', 'Prewitt', 'Roberts' and 'Sobel', perform very well when solely utilized in the keypoint-edge module compared with 'W/o'. Moreover, when unfixed operators

TABLE V
COMPARISON OF DIFFERENT EDGE OPERATORS IN KEYPOINT-EDGE CONSTRAINT. 'W/o' AND 'COMBINATION' IN THE FIRST COLUMN RESPECTIVELY REFER TO THE RESULTS WITHOUT APPLYING EDGE OPERATORS AND WITH ADAPTIVE EDGE FUSION (SHOWN IN SEC. III-B) DEPENDING ON FOUR UNFIXED OPERATORS.

Operator	Specificity	Sensitivity	Accuracy	AQE
W/o	93.18%	79.71%	87.26%	0.051 \pm 0.052
Laplacian	93.18%	79.71%	87.26%	0.050 \pm 0.050
Prewitt	92.05%	82.61%	87.90%	0.067 \pm 0.204
Roberts	94.32%	79.71%	87.90%	0.053 \pm 0.056
Sobel	95.45%	78.26%	87.90%	0.053 \pm 0.049
Combination	94.32%	81.16%	88.54%	0.050 \pm 0.050

(shown in Fig. 2(b)) are introduced for adaptively combining edges in 'Combination', whose performance can be further improved in terms of both accuracy and AQE. Specifically, 'Combination' outperforms 'Prewitt', 'Roberts' and 'Sobel'

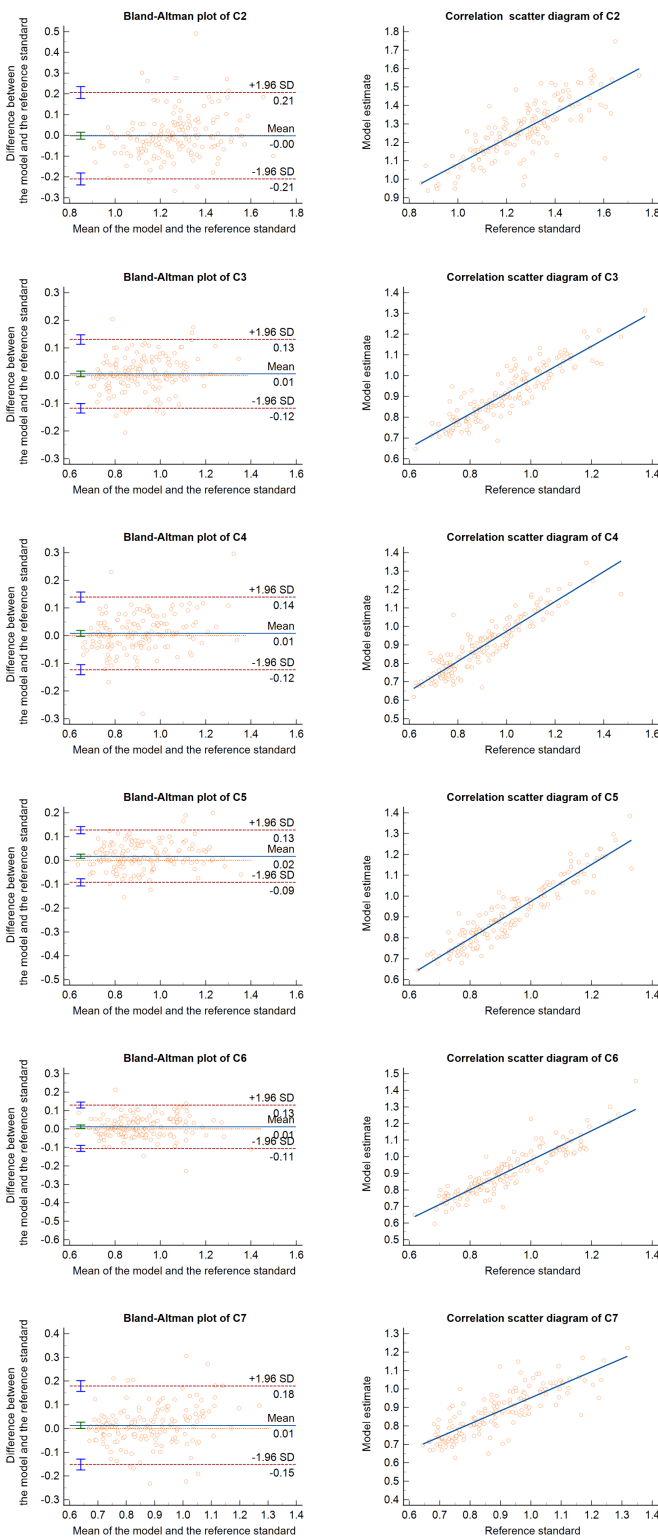


Fig. 4. Bland-Altman plots (left) and correlation scatter diagrams (right) show the difference and correlation between predicted and groundtruth SDD/VBD values.

as expected, achieving an improvement of 0.64 percentage point in accuracy. Meanwhile, it obtains the best AQE same as 'Laplacian'. Given that the high performance of accuracy and AQE achieved by incorporating keypoint-edge constraint with different operators, the improvement of 'Combination' is quite promising. These results demonstrate the effectiveness of applying different edge operators in keypoint-edge module and the superiority of adaptively fusing edges with unfixed operators to balance accuracy and AQE.

VI. CONCLUSION

This article introduces a topology-inspired network designed to address vertebral tasks across image and coordinate domains. The proposed network includes a keypoint-edge constraint module, ensuring that keypoints align with vertebral edges in the image domain, and a reparameterization block to rectify abnormal connected structures by combining both image and coordinate domains. Furthermore, compared to relying solely on coordinates or heatmaps, this cross-domain approach harnesses the spatial generalization of heatmaps along with the precise location information of coordinates, leading to enhanced accuracy in vertebral quantification. Extensive experimental results validate the superiority and applicability of the proposed network.

We believe that the keypoint-based network holds the potential to extend more nuanced topological insights to a range of vertebral quantification tasks. Moreover, the insights drawn from our work could potentially enhance the accuracy of other morphological parameters, precisely computed through alternative annotations like segmentation or frames.

REFERENCES

- [1] V. C. Hinck, P. D. Gordy, and H. E. Storino, "Developmental stenosis of the cervical spinal canal: radiological considerations," *Neurology*, vol. 14, no. 9, pp. 864–864, 1964.
- [2] H. Nakashima, Y. Yukawa, K. Suda, M. Yamagata, T. Ueta, and F. Kato, "Narrow cervical canal in 1211 asymptomatic healthy subjects: the relationship with spinal cord compression on mri," *European Spine Journal*, vol. 25, pp. 2149–2154, 2016.
- [3] S. Yamaguchi, T. Mitsuhashi, M. Abiko, M. Takeda, and K. Kurisu, "Epidemiology and overview of the clinical spectrum of degenerative cervical myelopathy," *Neurosurgery Clinics*, vol. 29, no. 1, pp. 1–12, 2018.
- [4] H. Yamahata, T. Niijo, M. Mori, S. Yamaguchi, M. Yonenaga, J. Sugata, T. Hiwatari, T. Okada, M. Atsushi, K. Arita *et al.*, "Is the atlas size associated with the pathophysiology of symptomatic spinal canal stenosis at the c1 level?" *Journal of Clinical Neuroscience*, vol. 57, pp. 58–62, 2018.
- [5] M. J. Lee, E. H. Cassinelli, and K. D. Riew, "Prevalence of cervical spine stenosis: anatomic study in cadavers," *JBJS*, vol. 89, no. 2, pp. 376–380, 2007.
- [6] J.-K. Lim and H.-K. Wong, "Variation of the cervical spinal torg ratio with gender and ethnicity," *The Spine Journal*, vol. 4, no. 4, pp. 396–401, 2004.
- [7] A. Zakharov, M. Pisov, A. Bukharaev, A. Petraikin, S. Morozov, V. Gombolevskiy, and M. Belyaev, "Interpretable vertebral fracture quantification via anchor-free landmarks localization," *Medical Image Analysis*, vol. 83, p. 102646, 2023.
- [8] T. Kim, Y.-G. Kim, S. Park, J.-K. Lee, C.-H. Lee, S.-J. Hyun, C. H. Kim, K.-J. Kim, and C. K. Chung, "Diagnostic triage in patients with central lumbar spinal stenosis using a deep learning system of radiographs," *Journal of Neurosurgery: Spine*, vol. 37, no. 1, pp. 104–111, 2022.

[9] H. Wu, C. Bailey, P. Rasoulinejad, and S. Li, "Automatic landmark estimation for adolescent idiopathic scoliosis assessment using boostnet," in *Medical Image Computing and Computer Assisted Intervention-MICCAI 2017: 20th International Conference, Quebec City, QC, Canada, September 11-13, 2017, Proceedings, Part I 20*. Springer, 2017, pp. 127–135.

[10] Z. Wang, J. Lv, Y. Yang, Y. Lin, Q. Li, X. Li, and X. Yang, "Accurate scoliosis vertebral landmark localization on x-ray images via shape-constrained multi-stage cascaded cnns," *Fundamental Research*, 2022.

[11] J. Yi, P. Wu, Q. Huang, H. Qu, and D. N. Metaxas, "Vertebra-focussed landmark detection for scoliosis assessment," in *2020 IEEE 17th International Symposium on Biomedical Imaging (ISBI)*. IEEE, 2020, pp. 736–740.

[12] C. Zhang, J. Wang, J. He, P. Gao, and G. Xie, "Automated vertebral landmarks and spinal curvature estimation using non-directional part affinity fields," *Neurocomputing*, vol. 438, pp. 280–289, 2021.

[13] W. Wu, C. Qian, S. Yang, Q. Wang, Y. Cai, and Q. Zhou, "Look at boundary: A boundary-aware face alignment algorithm," in *Proceedings of the IEEE Conference on Computer Vision and Pattern Recognition*, 2018, pp. 2129–2138.

[14] F. Wang, K. Zheng, L. Lu, J. Xiao, M. Wu, and S. Miao, "Automatic vertebra localization and identification in ct by spine rectification and anatomically-constrained optimization," in *Proceedings of the IEEE/CVF Conference on Computer Vision and Pattern Recognition*, 2021, pp. 5280–5288.

[15] J. Pan, H. Zhang, W. Wu, Z. Gao, and W. Wu, "Multi-domain integrative swin transformer network for sparse-view tomographic reconstruction," *Patterns*, vol. 3, no. 6, p. 100498, 2022.

[16] A. Nibali, Z. He, S. Morgan, and L. Prendergast, "Numerical coordinate regression with convolutional neural networks," *arXiv preprint arXiv:1801.07372*, 2018.

[17] M. Lin, Q. Chen, and S. Yan, "Network in network," in *ICLR*, 2014.

[18] D. Won, H.-J. Lee, S.-J. Lee, and S. H. Park, "Spinal stenosis grading in magnetic resonance imaging using deep convolutional neural networks," *Spine*, vol. 45, no. 12, pp. 804–812, 2020.

[19] J. Kim, S. Lee, E. Hwang, K. S. Ryu, H. Jeong, J. W. Lee, Y. Hwangbo, K. S. Choi, and H. S. Cha, "Limitations of deep learning attention mechanisms in clinical research: empirical case study based on the korean diabetic disease setting," *Journal of Medical Internet Research*, vol. 22, no. 12, p. e18418, 2020.

[20] Y. Zhan, D. Maneesh, M. Harder, and X. S. Zhou, "Robust mr spine detection using hierarchical learning and local articulated model," in *Medical Image Computing and Computer-Assisted Intervention-MICCAI 2012: 15th International Conference, Nice, France, October 1-5, 2012, Proceedings, Part I 15*. Springer, 2012, pp. 141–148.

[21] B. Glocker, D. Zikic, E. Konukoglu, D. R. Haynor, and A. Criminisi, "Vertebrae localization in pathological spine ct via dense classification from sparse annotations," in *Medical Image Computing and Computer-Assisted Intervention-MICCAI 2013: 16th International Conference, Nagoya, Japan, September 22-26, 2013, Proceedings, Part II 16*. Springer, 2013, pp. 262–270.

[22] Y. Chen, Y. Gao, K. Li, L. Zhao, and J. Zhao, "Vertebrae identification and localization utilizing fully convolutional networks and a hidden markov model," *IEEE Transactions on Medical Imaging*, vol. 39, no. 2, pp. 387–399, 2019.

[23] H. Liao, A. Mesfin, and J. Luo, "Joint vertebrae identification and localization in spinal ct images by combining short-and long-range contextual information," *IEEE Transactions on Medical Imaging*, vol. 37, no. 5, pp. 1266–1275, 2018.

[24] C. Qin, D. Yao, H. Zhuang, H. Wang, Y. Shi, and Z. Song, "Residual block-based multi-label classification and localization network with integral regression for vertebrae labeling," *arXiv preprint arXiv:2001.00170*, 2020.

[25] J. Gu, H. Kwon, D. Wang, W. Ye, M. Li, Y.-H. Chen, L. Lai, V. Chandra, and D. Z. Pan, "Multi-scale high-resolution vision transformer for semantic segmentation," in *Proceedings of the IEEE/CVF Conference on Computer Vision and Pattern Recognition*, 2022, pp. 12094–12103.

[26] X. Wang, L. Bo, and L. Fuxin, "Adaptive wing loss for robust face alignment via heatmap regression," in *Proceedings of the IEEE/CVF international conference on computer vision*, 2019, pp. 6971–6981.

[27] J. Xie, J. Wan, L. Shen, and Z. Lai, "Think about boundary: Fusing multi-level boundary information for landmark heatmap regression," in *2021 International Joint Conference on Neural Networks (IJCNN)*. IEEE, 2021, pp. 1–8.

[28] Z. Jin, X. Li, Y. Zhang, L. Shen, Z. Lai, and H. Kong, "Boundary regression-based reep neural network for thyroid nodule segmentation in ultrasound images," *Neural Computing and Applications*, pp. 1–10, 2022.

[29] O. Ronneberger, P. Fischer, and T. Brox, "U-net: Convolutional networks for biomedical image segmentation," in *Medical Image Computing and Computer-Assisted Intervention-MICCAI 2015: 18th International Conference, Munich, Germany, October 5-9, 2015, Proceedings, Part III 18*. Springer, 2015, pp. 234–241.

[30] K. He, X. Zhang, S. Ren, and J. Sun, "Deep residual learning for image recognition," in *Proceedings of the IEEE conference on computer vision and pattern recognition*, 2016, pp. 770–778.

[31] J. Long, E. Shelhamer, and T. Darrell, "Fully convolutional networks for semantic segmentation," in *Proceedings of the IEEE conference on computer vision and pattern recognition*, 2015, pp. 3431–3440.

[32] Y. Yuan, R. Fu, L. Huang, W. Lin, C. Zhang, X. Chen, and J. Wang, "Hrformer: High-resolution vision transformer for dense predict," *Advances in Neural Information Processing Systems*, vol. 34, pp. 7281–7293, 2021.

[33] A. Dosovitskiy, L. Beyer, A. Kolesnikov, D. Weissenborn, X. Zhai, T. Unterthiner, M. Dehghani, M. Minderer, G. Heigold, S. Gelly *et al.*, "An image is worth 16x16 words: Transformers for image recognition at scale," *arXiv preprint arXiv:2010.11929*, 2020.

[34] J. Li, T. Chen, R. Shi, Y. Lou, Y.-L. Li, and C. Lu, "Localization with sampling-argmax," *Advances in Neural Information Processing Systems*, vol. 34, pp. 27236–27248, 2021.

[35] E. Jang, S. Gu, and B. Poole, "Categorical reparameterization with gumbel-softmax," in *International Conference on Learning Representations*, 2017.

[36] G. Huang, Z. Liu, L. Van Der Maaten, and K. Q. Weinberger, "Densely connected convolutional networks," in *Proceedings of the IEEE conference on computer vision and pattern recognition*, 2017, pp. 4700–4708.

[37] S. Ioffe and C. Szegedy, "Batch normalization: Accelerating deep network training by reducing internal covariate shift," in *International conference on machine learning*. pmlr, 2015, pp. 448–456.

[38] Y. Chen, Z. Wang, Y. Peng, Z. Zhang, G. Yu, and J. Sun, "Cascaded pyramid network for multi-person pose estimation," in *Proceedings of the IEEE conference on computer vision and pattern recognition*, 2018, pp. 7103–7112.

[39] K. Sun, B. Xiao, D. Liu, and J. Wang, "Deep high-resolution representation learning for human pose estimation," in *Proceedings of the IEEE/CVF Conference on Computer Vision and Pattern Recognition*, 2019, pp. 5693–5703.

[40] L. Wang, C. Xie, Y. Lin, H.-Y. Zhou, K. Chen, D. Cheng, F. Dubost, B. Collery, B. Khanal, B. Khanal *et al.*, "Evaluation and comparison of accurate automated spinal curvature estimation algorithms with spinal anterior-posterior x-ray images: The aasce2019 challenge," *Medical Image Analysis*, vol. 72, p. 102115, 2021.

[41] L. Wang, Q. Xu, S. Leung, J. Chung, B. Chen, and S. Li, "Accurate automated cobb angles estimation using multi-view extrapolation net," *Medical Image Analysis*, vol. 58, p. 101542, 2019.

[42] M.-H. Horng, C.-P. Kuok, M.-J. Fu, C.-J. Lin, Y.-N. Sun *et al.*, "Cobb angle measurement of spine from x-ray images using convolutional neural network," *Computational and mathematical methods in medicine*, vol. 2019, 2019.

[43] C. Lukas, B. Jian, L. F. Rodriguez Venegas, F. De Benetti, S. Ruehling, A. Sekuboyina, J. Gempt, J. S. Kirschke, M. Piraud, J. Oberreuter *et al.*, "Patient-specific virtual spine straightening and vertebrae inpainting: An automatic framework for osteoplasty planning," in *Medical Image Computing and Computer Assisted Intervention-MICCAI 2021: 24th International Conference, Strasbourg, France, September 27–October 1, 2021, Proceedings, Part IV 24*. Springer, 2021, pp. 529–539.

[44] S. Pang, C. Pang, Z. Su, L. Lin, L. Zhao, Y. Chen, Y. Zhou, H. Lu, and Q. Feng, "Dgmsnet: Spine segmentation for mr image by a detection-guided mixed-supervised segmentation network," *Medical Image Analysis*, vol. 75, p. 102261, 2022.

[45] C. Payer, D. Stern, H. Bischof, and M. Urschler, "Integrating spatial configuration into heatmap regression based cnns for landmark localization," *Medical image analysis*, vol. 54, pp. 207–219, 2019.

[46] D. P. Kingma and J. Ba, "Adam: A method for stochastic optimization," *arXiv preprint arXiv:1412.6980*, 2014.